DOI: 10.1002/ejic.200800837

Structural, ^{103}Rh NMR and DFT Studies of a Bis(phosphane)Rh^{III}–Porphyrin Derivative

Orde Q. Munro,*[a] Greville L. Camp,[a] and Laurence Carlton[b]

Keywords: ^{103}Rh NMR spectroscopy / Porphyrin / Density functional calculations / GIAO / Phosphanes

The synthesis and characterisation of a novel bis(phosphane)-rhodium(III)–porphyrin, $[Rh(TPP)(PEtPh_2)_2]SbF_6$ (compound **1**; TPP = dianion of 5,10,15,20-tetraphenylporphyrin) is described. The X-ray structure of the bis(dichloromethane) solvate of the complex has a moderately ruffled porphyrin core conformation, which is primarily determined by the relative orientations of the axial phosphane ligands and their steric interaction with the porphyrin phenyl rings. The mean Rh–N and Rh–P bond lengths for **1** are 2.036(5) and 2.401(3) Å, respectively. The mean absolute perpendicular displacements of the porphyrin α-, β- and *meso*-carbon atoms from the 24-atom porphyrin mean plane measure 0.15(3), 0.11(8) and 0.27(2) Å, respectively. The ^{103}Rh NMR chemical shifts of **1**, determined by means of indirect detection through polarisation transfer from ^{31}P, were δ = 2480, 2558 and 2590 ppm at 213, 300 and 333 K, respectively. The ^{31}P chemical shifts measured δ = 10.68, 10.79 and 10.84 ppm at the same temperatures. Ruffled and planar porphyrin conformations are possible for **1** and were modelled by using DFT simulations at the PBE1PBE/3-21G** level of theory with the cation $[Rh(TPP)(PEtPh_2)_2]^+$. Accurate structural parameters (calculated bond lengths and out-of-plane porphyrin core atom displacements within 2 % and 0.02 Å of the experimental values, respectively) and moderately accurate ^{103}Rh isotropic shielding tensors ($\delta_{Rh}^{calcd.}$ within 13 % of $\delta_{Rh}^{exp.}$ at 0 K using the GIAO method) were calculated with this hybrid functional and relatively small all-electron basis set. The DFT simulations indicate unusually high fractional electron populations for the formally antibonding $4d_{z^2}$ and $4d_{x^2-y^2}$ orbitals of both the ruffled and planar conformers of $[Rh(TPP)(PEtPh_2)_2]^+$, consistent with the relatively low energies of these metal-character orbitals that are evidently well-mixed with ligand orbitals.

Introduction

From a structural standpoint, group 7–9 metalloporphyrins with P-donor axial ligands have not been as extensively characterised as their N-donor axial ligand counterparts. The majority of the reported structures are six-coordinate 18-electron Ru^{II} complexes such as $[Ru(OEP)(PPh_3)_2]$,[1,2] $[Ru(OEP)Br(PPh_3)]$,[3] $[Ru(TF_5PP)(PPh_3)_2]$[4] and other porphyrins with elaborate axial phosphane ligands [e.g. diphenyl(2-phenylethynyl)phosphane].[5] Structures of the isoelectronic low-spin Fe^{II} complexes typified by $[Fe(OEP)(PMe_3)_2]$ and $[Fe(TPP)(PBu_3)_2]$[6] are also known, not only with simple phosphanes but also with phosphites such as $P(OMe)_3$.[7] These Fe^{II} complexes all have planar porphyrin core conformations. The analogous bis(phosphonite)Fe^{III} derivatives have ruffled porphyrin conformations with $P(OMe)_2Ph$ and $P(OEt)_2Ph$ as axial ligands,[8] whereas the bis(phosphane) derivative $[Fe(TPP)(PMe_2Ph)_2]ClO_4$ exhibits a planar porphyrin core conformation.[9] Of the 4d and 5d elements within groups 7–9, a 17-electron Re^{II} derivative has been structurally characterised and only a small number of 18-electron Os^{II}[10] and Ir^{III}[11] complexes such as $[Os(TPP)(PPh_3)_2]$[10a] have been reported. The analogous 18-electron Rh^{III} complexes have, similarly, not been extensively characterised, and only five X-ray structure determinations have been reported,[12] the most recent study illustrating the elegant use of Rh^{III}–porphyrins as building blocks for the construction of supramolecular arrays.[13]

Eighteen-electron Rh^{III}–porphyrins undergo ligand exchange reactions and anions such as iodide (but not methylide or chloride) may be substituted by phosphanes and related P-donor ligands.[13a] (Hydrido)Rh^{III} derivatives are reactive toward RCHO insertions,[14] simple (chlorido)-Rh^{III}–porphyrins are good photocatalysts for alcohol dehydrogenation reactions,[15] whereas other Rh^{III}–porphyrins efficiently catalyse the decomposition of ethyl diazoacetate and the transfer of (ethoxycarbonyl)carbene to generate cyclopropane derivatives.[16] The electrochemical behaviour of $[Rh(TPP)(PR_3)_2]PF_6$ salts, where R is an alkyl or aryl group, has been studied and is characterised by the formation of reactive Rh^{III} π anion radicals or the Rh^{II} dimer

[a] School of Chemistry, University of KwaZulu-Natal, Private Bag X01, Scottsville, 3209, Pietermaritzburg, South Africa
Fax: +27-33-260-5009
E-mail: MunroO@ukzn.ac.za
[b] School of Chemistry, University of the Witwatersrand, P. O. Wits 2050, Johannesburg, South Africa
Fax: +27-11-717-6749
E-mail: Laurence.Carlton@wits.ac.za

Supporting information for this article is available on the WWW under http://www.eurjic.org/ or from the author.

[(TPP)Rh]$_2$.[17] Interestingly, sterically hindered phosphanes such as PPh_3 bind fairly strongly to Rh^{III}–porphyrins {logK^{293K} ≈ 3.1 for substitution of the solvent ligand in [Rh(TPP)(PPh_3)(THF)]$^+$}.[17a]

Despite the increasing importance of Rh^{III}–porphyrins in catalysis and coordination chemistry, none have been characterised by ^{103}Rh NMR spectroscopy,[18] a situation that reflects the experimental difficulties associated with direct detection of this I = ½ nucleus.[19,20] Most studies on simple Rh complexes have therefore employed indirect detection[21] of the ^{103}Rh nucleus in double- or triple-resonance HMQC experiments by employing polarisation transfer from ^{31}P, ^{1}H or ^{11}B.[22] Given that the Rh^{III}–porphyrins investigated hitherto[13,23] have not been probed by ^{103}Rh NMR spectroscopy, we describe here the first combined ^{103}Rh NMR and DFT study of a phosphane-ligated Rh^{III}–porphyrin, namely [Rh(TPP)(PEtPh_2)$_2$]SbF_6 (**1**, Scheme 1). Compound **1** has, moreover, been characterised by single-crystal X-ray diffraction as its bis(dichloromethane) solvate. The geometries, electronic structures and NMR shielding tensors of the planar and ruffled conformational isomers of [Rh(TPP)(PEtPh_2)$_2$]$^+$ have been determined by DFT and DFT-GIAO methods to (i) establish their relative energies and (ii) to gain a fundamental description of the electronic structure of the Rh^{III} ion in a porphyrin-based N_4P_2 ligand field.

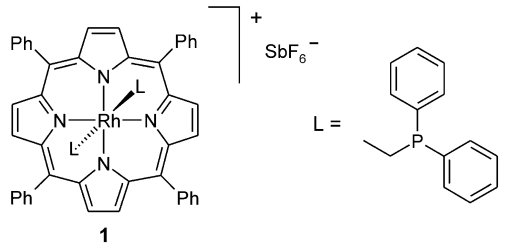

Scheme 1.

Results and Discussion

Synthesis and Crystallography

Metalloporphyrin **1** was synthesised by treating [Rh(TPP)Cl] with $AgSbF_6$ in dry THF to generate [Rh(TPP)(THF)$_2$]SbF_6 in situ prior to removal of the solvent in vacuo and treatment of this labile intermediate with an excess of ethyldiphenylphosphane (PEtPh_2) in dry dichloromethane. The X-ray crystal structure of **1**·2CH_2Cl_2 is shown in Figure 1. The porphyrin ligand exhibits a predominantly ruffled core conformation with mean absolute perpendicular displacements of the Rh, nitrogen and porphyrin α-, β- and *meso*-carbon atoms of 2(0), 2(2), 0.15(3), 0.11(8) and 0.28(1) Å, respectively. The porphyrin is thus moderately distorted from planarity (Figure 2).[24] The modest ruffling (porphyrin *meso*-carbon atoms alternately displaced above and below the 24-atom mean plane) presumably reflects the rather long mean axial Rh–P coordination distance of 2.401(3) Å and thus somewhat diminished steric interactions between the coordinated phosphane ligands and the porphyrin ring. Other Rh^{III} complexes with a *trans*-RhN_4P_2 coordination group and sterically hindered phosphane ligands exhibit similar axial bond lengths to **1**, for example [Rh($NCCH_3$)$_3$(NO)(PPh_3)$_2$]SbF_6[25] [Rh–P 2.404(3) Å] and [Rh(TPP)(PPh_2{CCC_6H_5})$_2$]I·($CHCl_3$) [Rh–P 2.371(2) Å].[26]

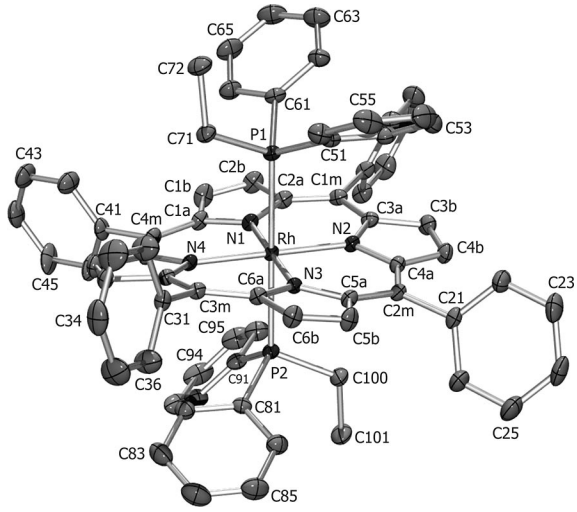

Figure 1. Selectively labelled thermal ellipsoid diagram[64] of the X-ray crystal structure of **1**·2(CH_2Cl_2). H atoms, solvent molecules and the counterion have been omitted for clarity (30% ellipsoid probabilities are shown). Key bond lengths [Å] and angles [°]: Rh–N1 2.035(3), Rh–N2 2.033(3), Rh–N3 2.043(3), Rh–N4 2.031(3), Rh–P1 2.3986(13), Rh–P2 2.4031(13), N1–Rh–P1 90.5(1), N1–Rh–P2 91.5(1); P1–Rh–P2 177.96(4), C51–P1–Rh 112.1(2), C71–P1–Rh 112.3(2), C61–P1–Rh 116.3(2), C81–P2–Rh 112.2(1), C100–P2–Rh 112.1(2), C91–P2–Rh, 116.9(2).

The long Rh–P bond for **1** differs substantially from the short [2.306(3) Å] distance reported for [Rh(OEP)Cl(PPh_3)]·2($CHCl_3$).[27] The shorter Rh–P distance of the latter complex reflects the fact that the Rh^{III} ion is displaced out of the porphyrin mean plane towards the single PPh_3 ligand, which permits a closer interaction with PPh_3, even though PPh_3 (Tolman's[28] cone angle = 145°) is sterically more hindered than the PEtPh_2 ligands of **1** (cone angle = 140°). The average Rh–N distance for **1** is more typical for a metalloporphyrin at 2.036(5) Å and is experimentally equivalent (within 3σ) to that seen in [Rh(OEP)Cl(PPh_3)] [2.024(35) Å].[28] Although the porphyrin *meso*-phenyl groups are canted relative to the 24-atom porphyrin mean plane (dihedral angles = 65.6, 64.1, 82.8 and 74.2° for the Ph groups appended to *meso*-carbon atoms C1m through C4m, respectively), they do not significantly saddle[25] the already ruffled conformation of the porphyrin ring. This suggests that the conformation of **1** is probably largely governed by axial ligand···porphyrin core and axial ligand···porphyrin phenyl group nonbonding interactions, an effect confirmed by the DFT-calculated structure of **1** in the presence and absence of the porphyrin phenyl groups (vide infra).

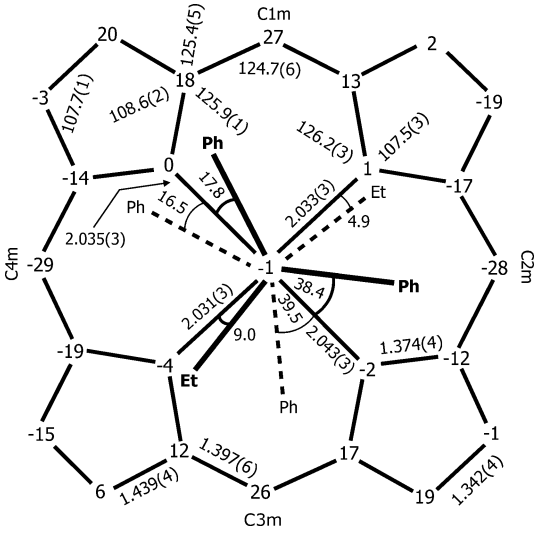

Figure 2. Formal diagram displaying the perpendicular displacements in units of 0.01 Å (esd = 0.003 Å) of the porphyrin ring atoms from the 24-atom mean plane of **1**·2(CH_2Cl_2). Chemically unique mean bond lengths [Å] and angles [°] as well as the relative orientations of the axial phosphane ligands are shown (heavy and dashed lines reflect the above- and below-plane axial ligands, respectively). Angles shown without esd's (for clarity) have an esd of 0.2°.

The aryl groups of the coordinated phosphane ligands adopt dihedral angles of 26.3(1), 35.4(1), 24.7(2) and 42.3(1)° relative to the porphyrin mean plane for the rings containing carbon atoms C51, C61, C81 and C91, respectively. For the phosphane phenyl rings C51–C56 and C81–C86, these dihedral angles are rather close to being parallel with the porphyrin ring. Indeed, there are several short phenyl ring···pyrrole ring intramolecular nonbonding contacts that point to the existence of stabilising intramolecular π–π interactions in **1**.[29] Interestingly, the axial phosphane ligands exhibit an approximate *anti* configuration, in which the ethyl substituents nearly eclipse the in-plane Rh–N bonds [N4–Rh–P1–C71 4.9(2)° and N2–Rh–P2–C100 10.3(2)°]. We believe that this relative orientation for the axial ligands in **1**, coupled with their significant steric bulk, might be responsible for the observed ruffled porphyrin conformation, particularly since we previously found [Co(TPP)(1-MepipZ)$_2$]SbF_6 (1-MepipZ = 1-methylpiperazine[1]) to be ruffled for similar reasons.[30]

Electronic Spectroscopy

The electronic absorption spectrum of **1** recorded in dry dichloromethane (Figure 3) over the full spectroscopic range is very similar to that reported by Kadish et al.[17a] for [Rh(TPP)(PPh_3)$_2$]PF_6 (λ_{max} = 448, 557, 597 nm) from 380–700 nm in the same solvent. The Soret (448 nm) and two sharply resolved *Q* bands (557, 597 nm) are markedly redshifted relative to those of the five-coordinate precursor [Rh(TPP)Cl]. Addition of solid KCN to the solution of **1** followed by equilibration of the heterogeneous mixture at room temperature for 12 h afforded the spectrum of K[Rh(TPP)$(CN)_2$] as a result of complete substitution of the $PEtPh_2$ ligands. The electronic spectrum of K[Rh(TPP)$(CN)_2$] shows the same number of bands and overall spectroscopic intensity pattern as **1**, particularly in the visible region, confirming that the spectroscopic features for **1** are consistent with a six-coordinate Rh^{III}–porphyrin. The main absorption maxima of K[Rh(TPP)$(CN)_2$] are, however, blueshifted relative to those of **1** (by up to 9 nm). One possible interpretation of the marked redshift for the *Q* and *B* bands of **1** relative to those of the dicyanido complex is that such a spectroscopic perturbation might well correlate with the order of CN^- and $PEtPh_2$ in the nephelauxetic series. Evidently, the softer axial ligand ($PEtPh_2$) favours a narrower HOMO–LUMO gap and consequently lower *Q* and *B* state energies.

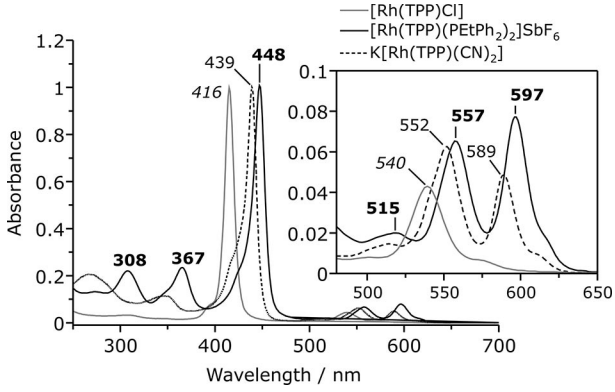

Figure 3. Normalised electronic spectra of selected Rh^{III}–porphyrins recorded in dry dichloromethane at 298 K. The inset shows an expansion of the visible spectra of the three complexes.

The foregoing argument is strongly supported by the spectroelectrochemical data of Kadish and co-workers[17a] which provide an experimental probe of the HOMO–LUMO gap from the one-electron redox reactions of related Rh^{III}–porphyrins. Specifically, [Rh(TPP)(PF_3)(OH)] has a Soret band maximum at 420 nm and $\Delta E_{HOMO-LUMO}$ = 2.29 V, whereas [Rh(TPP)$(PMePh_2)_2$]PF_6 has λ_{max} = 446 nm and $\Delta E_{HOMO-LUMO}$ = 2.22 V ($\Delta E_{HOMO-LUMO} = E_{½}^{ox} - E_{½}^{red}$). Note that the one-electron first oxidation and reduction reactions of these complexes involve the porphyrin ring and form π cation and π anion radicals, respectively. Clearly, an axial ligand combination high up in the nephelauxetic series correlates with a redshifted Soret band and narrower HOMO–LUMO gap.

One problem encountered during spectroscopic analysis of **1** was partial aquation of the complex if dry solvents were not employed. Indeed, addition of water-saturated dichloromethane to a solution of **1** in dry dichloromethane afforded a small saturating fraction of [Rh(TPP)(OH_2)-$(PEtPh_2)$]SbF_6 with an increase in the water content of the solution, as evidenced by the appearance of the *B* and *Q* bands at ca. 420 and 527 nm, respectively, bands that are characteristic of this species (Figure S1, Supporting Information). The ^1H NMR spectra of **1** recorded in $CDCl_3$ (Figures 5 and S3) also confirmed the presence of this species. Formation of a stable mixed-ligand Rh^{III}–porphyrin

derivative (P,O axial donor atom combination) is not without precedent. Specifically, Kadish and co-workers studied solvolysis of $[Rh(TPP)(PPh_3)_2]PF_6$ in THF which leads to the formation of the mixed-ligand complex $[Rh(TPP)(THF)(PPh_3)]PF_6$.[17a] Consistent with the aquation reaction here, formation of $[Rh(TPP)(THF)(PPh_3)]PF_6$ was characterised by the loss of the Soret band intensity at 448 nm, with concomitant appearance of a new Soret band for the mixed-ligand solvolysis product at 425 nm.[17a] We also found that $[Rh(TPP)(OH_2)(PEtPh_2)]SbF_6$ was the sole species in a dry dichloromethane solution if aged and powdered crystalline material was used for the preparation of the solution (Figure S2). The evidence suggests that powdered **1** is susceptible to aquation [specifically formation of the mono(aqua) complex], particularly since this problem could be averted if large single crystals of **1** were used for solution preparation in dry dichloromethane.

The strongly redshifted Soret band of **1** occurs in the visible spectroscopic region and this, in conjunction with narrow bandwidths (Table S1, Supporting Information), permits facile resolution of the *Q*, *B*, *N* and *L* electronic states[31] for the complex. As shown in Figure 4, the complete spectroscopic envelope could be deconvoluted into a number of constituent Voigt functions. The quantised vibrational levels of the *Q* state exhibit an energy separation of ca. 1203–1427 cm^{-1} based on the energies of the *Q*(0,0), *Q*(1,0) and *Q*(2,0) bands (16750, 17953 and 19380 cm^{-1}, respectively). The vibrational energy levels of the *B* state for **1** are more narrowly spaced (ca. 406–475 cm^{-1}). A distinctive spectroscopic feature for compound **1** is the markedly good resolution of the *N* and *L* bands at 367 and 309 nm, respectively. These bands are also present for $K[Rh(TPP)(CN)_2]$ but occur at slightly higher energy and are not as sharp or well-resolved as those of **1**. The longest-wavelength absorption band for compound **1** (615 nm) is ca. 1/7th of the intensity of the *Q*(0,0) band and, although of unknown orbital parentage, we note that a similar feature is found on the long-wavelength side of the *Q*(0,0) band for $K[Rh(TPP)(CN)_2]$. This feature is absent in [Rh(TPP)Cl].

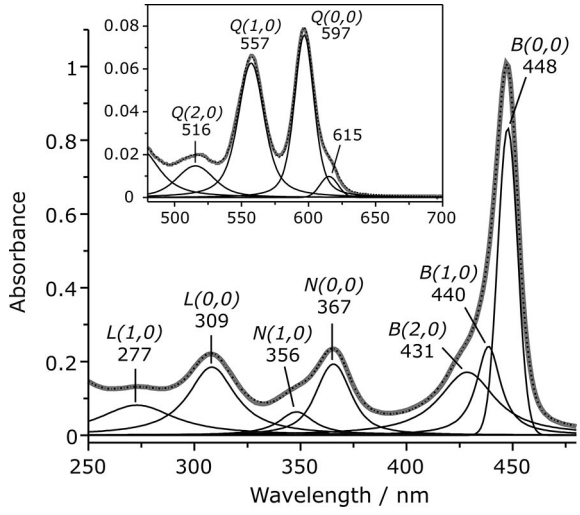

Figure 4. Deconvolution of the electronic spectrum of **1** into its constituent bands (Voigt functions, CH_2Cl_2, 298 K). The inset shows an expansion of the visible spectrum of the complex. The thick grey line is the experimental absorption envelope; the dashed line is the fit by the linear sum of the constituent bands (solid lines). Band maxima and assignments are given.

NMR Spectroscopy

^{1}H NMR Spectroscopic Data

An interesting question that arises for **1** is whether the relatively bulky axial ligands still allow dynamic exchange phenomena at ambient temperature. Inspection of the downfield region of the ^{1}H NMR spectrum of **1** (Figure 5) suggests that the axial phosphane ligands undergo free rotation about the Rh–P bonds leading to a single mean pyrrole β-proton resonance at δ = 8.810 ppm (a static configuration for the axial phosphanes would render the eight pyrrole β-protons inequivalent and hence split the signal). Furthermore, the pyrrole β-proton resonance changed negligibly from –20 °C (δ = 8.809 ppm) to 50 °C (δ = 8.814 ppm). Coupled with the fact that no NMR signals from free $PEtPh_2$ appeared at elevated temperatures, we conclude that dissociation of **1** to form the five-coordinate species $[Rh(TPP)(PEtPh_2)]SbF_6$ does not occur to any significant extent for $T \leq 50$ °C. The large magnetic anisotropy of the porphyrin ring current is also apparent in the ^{1}H NMR spectrum of **1**. Specifically, the axial ligand methylene protons exhibit a marked upfield shift from δ = 2.116 ppm in the free ligand to δ = –2.829 ppm in the Rh^{III}-bound ligand. Similarly, the ethyl group $-CH_3$ resonance shifts from δ = 1.147 to –1.388 ppm in the free and coordinated ligands, respectively. Finally, we note the marked 3.738 ppm ring current-induced shielding for the *ortho* protons of the axial ligand aryl groups as a result of their spatial projection towards the central core of the Rh^{III} porphyrin (the *o*-H signal shifts from δ = 7.484 to 3.746 ppm upon coordination of $PEtPh_2$ to $[Rh(TPP)]^+$ in the present solvent system). Similar porphyrin ring current induced shieldings are known for other low-spin d^6 metalloporphyrins.[31,32] From the ^{1}H NMR spectra of **1** above 253 K (Figure S4), the axial ligands and *meso*-phenyl groups are in the fast exchange limit on the 500 MHz NMR timescale.

The ^{1}H NMR spectrum of **1** (Figure 5) indicates a sample of acceptable purity (> 97%), although we did find evidence for two contaminant species *in solution*, namely ca. 0.7% of the mono(aqua) adduct, $[Rh(TPP)(OH_2)(PEtPh_2)]SbF_6$, and ca. 2–2.5% of a second bis(phosphane)Rh^{III}–porphyrin species with a distinct pyrrole proton signal at δ = 9.032 ppm (293 K). The identity of the latter minor component was difficult to establish. However, the variable-temperature ^{1}H NMR spectra for the system showed no evidence of an exchange equilibrium involving this species and **1**, suggesting that the minor component is not a conformational isomer of **1** but a separate six-coordinate Rh^{III}–porphyrin. As discussed below, we have assigned the minor species in the system to the complex [Rh(TPP)(PHEtPh)-

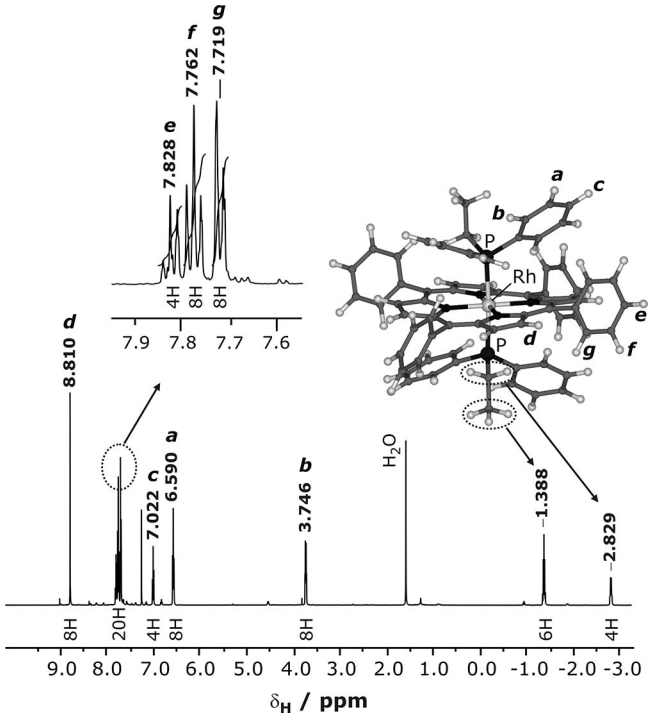

Figure 5. ^{1}H NMR spectrum and signal assignments for **1** ($CDCl_3$, 293 K). The minor species in solution (< 3%) was assigned with reasonable certainty to the mixed-ligand complex [Rh(TPP)(PHEtPh)($PEtPh_2$)]SbF_6 based on its observed and DFT-calculated ^{31}P and ^{103}Rh NMR spectra and the fact that PHEtPh is present (1.2%) in the commercial reagent ($PEtPh_2$) used to synthesise **1**.

($PEtPh_2$)]SbF_6 based on its ^{103}Rh and ^{31}P chemical shifts and the chemical shift of the P–H proton for the Rh-bound contaminant ligand (δ = –3.32 ppm). This diagnostic proton signal is shifted upfield relative to its chemical shift in the free ligand (δ_H = 5.66 ppm) upon coordination to Rh^{III}, consistent with marked shielding by the porphyrin ring current (see Supporting Information for spectroscopic details). The source of PHEtPh in the system, which is evidently present at a high enough concentration during the synthesis of **1** to give some of the mono(PHEtPh) adduct, was traced to the commercial reagent which is only 97.5% $PEtPh_2$.

Returning to the aquation adduct [Rh(TPP)(OH_2)($PEtPh_2$)]SbF_6, we found that the extent of equilibration to the monoaqua complex could be reduced, but not completely eliminated, by first passing the $CDCl_3$ used for solution preparation through a short column of activated alumina. This problem unfortunately persisted even when using clean crystalline material with good elemental analysis data for solution preparation. Unambiguous spectroscopic identification of [Rh(TPP)(OH_2)($PEtPh_2$)]SbF_6 is possible from the distinct, exchange-broadened, upfield ^{1}H resonance (δ = –4.8 ppm region, Figure S3) that shifts downfield with increasing temperature in an analogous fashion to signals of other protons in the molecule. The temperature dependence of the signal for the Rh^{III}–OH_2 protons [δ_H = –5.05(2) ppm + 8.0(7) × 10^4 ppm K^{-1} (T), correlation coefficient R = 0.993] is thus *opposite* to that for free water in the solvent. We also used the isotropic shielding tensor for the Rh–OH_2 protons calculated at the PBE1PBE/3-21G** level of theory by GIAO methods (δ = –5.63 ppm at 0 K) to confirm the experimentally observed strong shielding of the aqua ligand protons by the porphyrin ring current and thus the assignment of this signal/species in solution.

^{31}P and ^{103}Rh NMR Spectra

Proton-decoupled ^{103}Rh-^{31}P NMR spectra (2D) for **1** were obtained at three temperatures in $CDCl_3$ by using the classic pulse sequence described by Bax et al.[33] The 1D ^{31}P{^{1}H} and 2D ^{31}P-^{103}Rh{^{1}H} spectra for **1** are shown in Figure 6a and b, respectively. The ^{31}P NMR spectrum exhibits a distinct doublet consistent with spin coupling of the magnetically equivalent ^{31}P nuclei of the two $PEtPh_2$ ligands to the I = ½ ^{103}Rh nucleus. The ^{31}P-^{103}Rh coupling constant is most easily measured from the ^{31}P spectrum and has a value of 82.1 Hz at 300 K and an experimentally negligible temperature dependence from 213 to 333 K. As noted above, the ^{1}H NMR spectrum for **1** also showed the presence of [Rh(TPP)(PHEtPh)($PEtPh_2$)]SbF_6 (ca. 2–2.5%), a compound that is clearly structurally very similar to **1**. This species gave a ^{31}P doublet at δ = 13.3 ppm (300 K) and a ^{31}P-^{103}Rh coupling constant of 82.4 Hz that is clearly consistent with a six-coordinate complex.[17a] It was also evident in the ^{103}Rh NMR spectra of **1** (see Table S6 for chemical shifts as a function of T). Notwithstanding the inconsequentially small presence of both the monoaqua species and [Rh(TPP)(PHEtPh)($PEtPh_2$)]SbF_6, the 2D ^{31}P-^{103}Rh{^{1}H} spectrum for **1** at 300 K clearly shows two well-resolved cross peaks, consistent with spin-coupling of the two nuclei. Although the ^{31}P-^{103}Rh coupling is cleanly resolved in the ^{31}P{^{1}H} spectrum, the expected triplet resonance pattern is not resolved on the ^{103}Rh axis, consistent with observations for many simple Rh^{III} complexes.[34]

The ^{31}P chemical shifts were δ = 10.68, 10.79 and 10.84 ppm at 213, 300 and 333 K, respectively. The linear increase in δ_P with increasing temperature had a slope, intercept and correlation coefficient of 1.32(5) × 10^{-3} ppm K^{-1}, 10.40(2) ppm and 0.999, respectively. The ^{103}Rh chemical shifts were 2480, 2558 and 2590 ppm at 213, 300 and 333 K, respectively. The ^{103}Rh chemical shift therefore increases linearly with increasing temperature with a slope, intercept and correlation coefficient of 0.91(2) ppm K^{-1}, 2285(5) ppm and 0.9999, respectively. Interestingly, the temperature dependence of δ_{Rh} in **1** is roughly three times the value typically observed for simple Rh^{III} coordination compounds (slope ≈ 0.3–0.4 ppm K^{-1})[19] and is experimentally equivalent to that reported for *mer*-[$RhCl_3(SMe_2)_3$] [slope = 1.0(1) ppm K^{-1}].[19,35] Furthermore, the ^{103}Rh chemical shifts for **1** are upfield relative to those of simple Rh^{III} coordination compounds such as $[RhCl_6]^{3-}$ (δ_{Rh} = 8000 ppm)[19,36] but fall in the same range as those of *mer*-[$RhCl_3(PBu_3)_3$] (δ_{Rh} = 2770 ppm) and *mer*-[$RhCl_3(PMe_3)_3$]

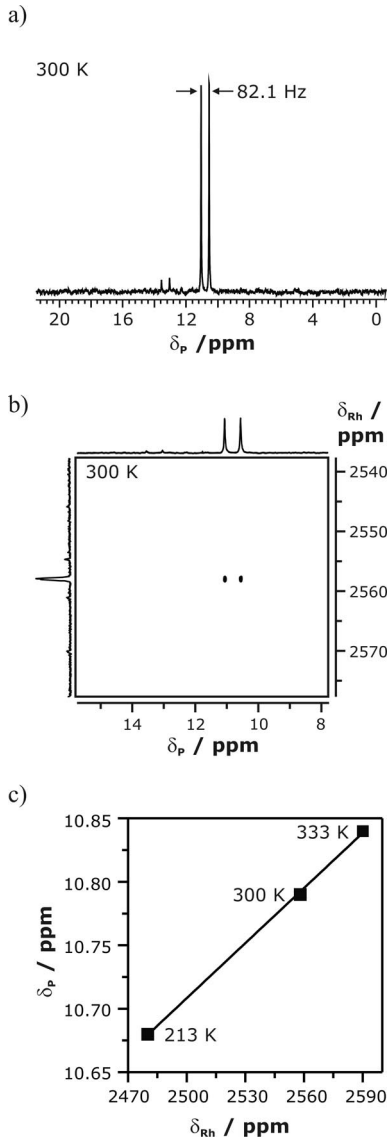

Figure 6. (a) ^{1}H-decoupled ^{31}P NMR spectrum of **1** in $CDCl_3$, (b) 2D ^{31}P-^{103}Rh{^{1}H} NMR spectrum of **1** and (c) plot of the ^{31}P and ^{103}Rh chemical shifts vs. temperature for **1**. The minor doublet component observed at δ_P = 13.3 ppm in the ^{31}P NMR spectrum of **1** has a similar $^{1}J_{Rh,P}$ coupling constant (82.4 Hz) to the major component and is therefore assigned to the less abundant (< 3%) six-coordinate mixed-ligand complex [Rh(TPP)(PHEtPh)-($PEtPh_2$)]SbF_6. The solution was 8 mM in concentration.

(δ_{Rh} = 2207 ppm).[19,37] Evidently, coordination of phosphane ligands by Rh^{III} increases the covalent nature of the complex and thus the shielding of the ^{103}Rh nucleus.

The variation of δ_P and δ_{Rh} with temperature may be explained with Equation (1), where ν_X, γ_X, B_0 and σ_X are the Larmor frequency, magnetogyric ratio, applied magnetic field and nuclear shielding constant for nuclide X, respectively.[19,38] The term σ_X in Equation (1) is given by Equation (2), where σ^d is the diamagnetic shielding constant (governed only by the core electron density), and the second term is the "paramagnetic" shielding constant, which depends on the charge density and bond order between nuclei X and Y (ΣQ_{XY}), the expectation value of the inverse cube of the non-s orbital radius ($\langle 1/r^3 \rangle$) and the inverse mean excitation energy for electronic transitions from the ground state (ΔE).[39]

$$\nu_X = \frac{\gamma_X}{2\pi} B_0(1 - \sigma_X) \quad (1)$$

$$\sigma_X = \sigma^d - \frac{\Sigma Q_{XY}}{\Delta E}\langle 1/r^3 \rangle \quad (2)$$

In the case of ^{31}P, ΔE is the mean singlet→triplet state excitation energy, which decreases slightly with increasing temperature due to the population of excited vibrational levels of the ground singlet state. This causes a slight increase in the Larmor frequency and thus δ_P with increasing temperature. A similar argument prevails for δ_{Rh} with the exception that ΔE in Equation (2) corresponds to the mean excitation energy for transitions involving the singlet state ligand field terms for the Rh^{III} ion. Because both nuclides exhibit temperature-dependent changes in chemical shifts of the same sign, a plot of δ_P vs. δ_{Rh} shows a linear trend with increasing temperature (Figure 6c) and succinctly summarises the changes in nuclear shielding for the two nuclides. Although Equation (2) is often invoked (with emphasis on the ΔE^{-1} parameter) to account for the temperature dependence of chemical shifts, one cannot exclude other explanations. The numerator term ΣQ_{XY} in Equation (2), in particular, is not insignificant for coordination compounds, because dative covalent bonds are more pliable than covalent bonds and thus deform more readily with changes in temperature and even the dielectric constant of the medium (which is also temperature-dependent). An interesting example of an alternative explanation of the large thermal shielding derivatives and NMR isotope shifts of many transition metal nuclei was put forward by Jameson et al.[39] using a model in which the derivatives of the nuclear shielding are dependent on the equilibrium M–L bond lengths according to a classical Morse-type function. This model was superior to Equation (2) because it not only accounted for chemical shift changes with temperature but also those that attend isotopic substitution in ML_6 complexes. Thus, coupled with changes in ground state vibrational energy level populations, the marked thermal shielding derivatives for the ^{31}P and ^{103}Rh nuclei of **1** probably also reflect rather complex changes in the mean Rh–N and Rh–P distances and internuclear charge densities with temperature.

DFT Calculations

In-vacuo DFT simulations at the PBE1PBE[40]/3-21G**[41] and PBE1PBE/DGDZVP[42] levels of theory were used to establish (a) the electronic structure, (b) the relative stabilities of the conformations of **1** with ruffled (*ruf*) and planar (*flat*) porphyrin macrocycles and (c) the ^{103}Rh and ^{31}P nuclear shielding tensors (by using the GIAO theory[43]) of the system. Simulations with the 3-21G** basis set were the most accurate for both the geometry and shielding tensor determinations (Figure 7 and Tables 1 and 4). For ex-

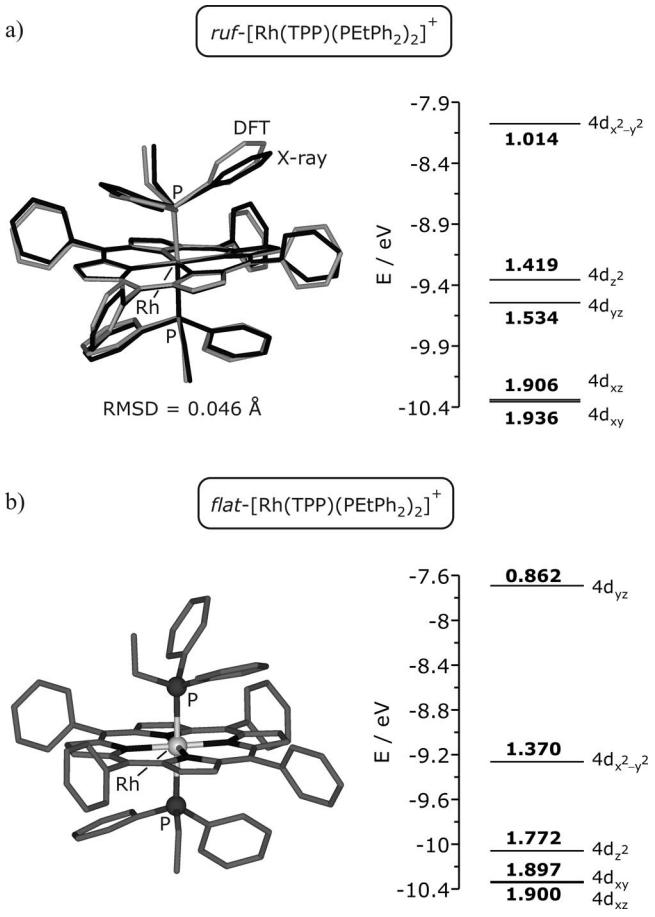

Figure 7. (a) Left: root mean square fit[65] of the X-ray cation of **1** (black) to the DFT-calculated C_1 symmetry geometry of *ruf*-$[Rh(TPP)(PEtPh_2)_2]^+$ at the PBE1PBE/3-21G** level of theory (grey). Right: 4d orbital energy levels and electron populations (NBO method) for the calculated cation structure on the left. (b) Left: DFT-calculated C_2 symmetry geometry of *flat*-$[Rh(TPP)(PEtPh_2)_2]^+$ (PBE1PBE/3-21G**). Right: 4d orbital energy levels and electron populations (NBO method) for the calculated cation structure on the left. H atoms have been omitted for clarity in all structures.

ample, bond lengths for the coordination group were within 0.6% of those determined crystallographically with the gradient-corrected PBE1PBE hybrid functional. Interestingly, the in vacuo geometry of *ruf*-$[Rh(TPP)(PEtPh_2)_2]^+$ was slightly less distorted than that observed crystallographically (cf. the conformational parameter $|C_m|$ in Table 1), presumably because of the omission of neighbouring molecules (i.e. crystal-packing effects) during the DFT simulations. Indeed, it is noteworthy that crystal packing induced distortions of axial and porphyrin ligand substituents are well-known determinants of the molecular conformation.[44] Simulations carried out on the *ruf* conformer of cationic **1** without the *meso*-phenyl groups of the porphyrin, i.e. by using a simple porphine model (data not shown), afforded good agreement between crystallographic and calculated bond lengths but poorer agreement between the observed and calculated porphyrin ring conformations. This suggests that intramolecular steric interactions (especially porphyrin-aryl···phosphane-aryl van der Waals interactions) play a role alongside axial-ligand···porphyrin-core nonbonded interactions in shaping the experimentally observed ruffled conformation of **1**.

Population Analysis

NBO analysis[45] of the converged wave function for the optimised geometry of *ruf*-$[Rh(TPP)(PEtPh_2)_2]^+$ reflects the formal low-spin $4d^6$ electron configuration for the system (Figure 7). It is, however, noteworthy (Table 2) that the valence-electron population of the Rh^{III} ion substantially exceeds 6 electrons presumably due to σ-donation from the porphyrin and axial phosphane ligands and substantial mixing of the metal and ligand orbitals (significant covalency), as shown in Figure 8. Indeed, the electron occupancies of the σ-antibonding MOs with significant $4d_{z^2}$ and $4d_{x^2-y^2}$ character far exceed zero, contrary to expectations from simple ligand-field arguments. Well-mixed metal and ligand orbitals for *ruf*-$[Rh(TPP)(PEtPh_2)_2]^+$ apparently allow excess electron density donated to the metal ion to be housed by the σ* MOs as these metal-character orbitals are

Table 1. Comparison of selected geometrical parameters for the experimental and DFT-calculated *ruf* and *flat* conformers of cationic **1**.[a]

	Exp.	3-21G**, *ruf*	Diff.[d]	3-21G**, *flat*	DGDZVP, *ruf*	Diff.[d]
Rh–N_p[b]	2.036(5)	2.043(6)	–0.007	2.046(7)	2.051(4)	–0.019
Rh–P	2.401(3)	2.392(4)	–0.009	2.399(0)	2.452(2)	–0.056
C_a–N_p	1.374(4)	1.381(2)	–0.007	1.381(1)	1.369(1)	0.008
C_b–C_a	1.439(4)	1.449(1)	–0.010	1.448(1)	1.441(1)	–0.003
C_b–C_b	1.342(4)	1.365(1)	–0.023	1.365(2)	1.361(1)	–0.020
C_a–C_m	1.397(6)	1.396(1)	0.001	1.395(2)	1.404(1)	0.003
|Rh|[c]	0.01(0)	0.00(0)	0.01	0.00(0)	0.00(0)	0.01
|N|	0.02(2)	0.02(1)	0	0.03(2)	0.02(1)	0.02
$\|C_a\|$	0.15(3)	0.14(2)	0.01	0.04(3)	0.12(3)	0.07
$\|C_b\|$	0.11(8)	0.10(6)	0.01	0.10(4)	0.09(8)	0.05
$\|C_m\|$	0.27(2)	0.25(1)	0.02	0.02(4)	0.22(1)	0.13
P–Rh–P	177.96(4)	176.0	0	177.2	176.4	–1.46

[a] DFT method = PBE1PBE; distances in Å, angles in °. [b] N_p, C_a, C_b, and C_m = porphyrin nitrogen, α-, β-, and *meso*-carbon, respectively. [c] |X|: mean absolute perpendicular displacement of atom type X from the 24-atom porphyrin mean plane. [d] Difference relative to the experimental value.

particularly low-lying in energy. This phenomenon is evident for both conformations of cationic **1** but perhaps best illustrated in the case of *ruf*-[Rh(TPP)($PEtPh_2$)$_2$]$^+$ where the $4d_{z^2}$ orbital exhibits a population of ca. 1.4 *e* due to its rather low energy (< –9.3 eV; Figure 7) for an otherwise somewhat atypical "rhombic symmetry" metalloporphyrin d-orbital energy-level sequence (the typical d-orbital energy-level sequence for low-spin ferric porphyrins axially ligated by a pair of strong-field ligands, for example, is: $d_{xy} < d_{xz} < d_{yz} < d_{x^2-y^2} < d_{z^2}$).[46]

Table 2. Key NBO charge and electron populations for the conformations of [Rh(TPP)($PEtPh_2$)$_2$]$^+$ with ruffled and planar porphyrin cores calculated at the PBE1PBE/3-21G** level of theory.

Atom	Charge	Core	Valence	Rydberg	Total
Ruffled (C_1 symmetry)					
Rh	0.783	35.985	8.170	0.063	44.217
N	–0.493	1.999	5.487	0.007	7.493
N	–0.502	1.999	5.495	0.007	7.502
N	–0.502	1.999	5.496	0.007	7.502
N	–0.502	1.999	5.496	0.007	7.502
P	1.138	9.997	3.802	0.064	13.862
P	1.145	9.997	3.795	0.064	13.855
Planar (C_2 symmetry)[a]					
Rh	0.792	35.985	8.162	0.061	44.208
N	–0.496	1.999	5.490	0.007	7.496
N	–0.504	1.999	5.498	0.007	7.504
P	1.138	9.997	3.802	0.064	13.862

[a] Only the symmetry-unique charges are shown.

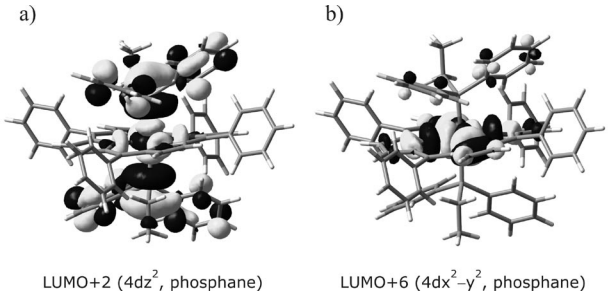

Figure 8. Mixing of the formally σ antibonding 4d metal and ligand orbitals for *ruf*-[Rh(TPP)($PEtPh_2$)$_2$]$^+$. (a) Antibonding MO with ca. 18% $4d_{z^2}$ character. (b) Antibonding MO with ca. 45% $4d_{x^2-y^2}$ character.

The markedly different 4d-orbital energy-level sequence for *flat*-[Rh(TPP)($PEtPh_2$)$_2$]$^+$ relative to that of *ruf*-[Rh(TPP)($PEtPh_2$)$_2$]$^+$ appears odd at first glance (Figure 7), particularly the observation that the highest-energy metal-character MO in *ruf*-[Rh(TPP)($PEtPh_2$)$_2$]$^+$ ($4d_{x^2-y^2}$) differs from that in *flat*-[Rh(TPP)($PEtPh_2$)$_2$]$^+$ ($4d_{yz}$). This change in the energy order of the 4d orbitals merely reflects the fact that the Cartesian axes have different orientations relative to the RhN_4P_2 coordination sphere framework in the two conformers (as shown in Figure S8), a situation that is probably chemically inconsequential but nonetheless of some theoretical interest. One worthwhile comment on the NBO population analysis for the two conformers of [Rh(TPP)($PEtPh_2$)$_2$]$^+$ is the lack of any real difference in the partial atomic charges and valence-electron populations of the RhN_4P_6 coordination sphere (Table 2). However, the slightly lower partial atomic charge and slightly higher valence-electron population for Rh in *ruf*-[Rh(TPP)($PEtPh_2$)$_2$]$^+$ probably reflects the marginally shorter Rh–N and Rh–P distances (Table 1). The Rydberg populations of the Rh-bound P atoms (0.064 *e* in both conformers) are significantly higher than that of free $PEtPh_2$ (0.042 *e*, calculated at the same level of theory in vacuo) and likely reflect at least some quantifiable backbonding from Rh to P. The exact nature of the backbonding interaction is difficult to establish with certainty from the present data but could involve either one or more vacant 3d orbitals on P or indeed a σ*-type MO on the phosphane ligand. From the full NBO atomic orbital population analysis data given in Table S2, we find that the 4p (Rydberg) orbitals of phosphorus in $PEtPh_2$ gain the most electron density upon coordination of the ligand to Rh^{III}, suggesting that the 3d orbitals of P are not the dominant M→L electron-transfer destination for either conformer of **1**. Lastly, the partial positive charge on P exceeds that on Rh^{III} and that of the metal-free ligand in the gas phase (0.917 *e*), a situation that strikingly highlights the significant covalency of the Rh–P bonds in contrast to the Rh–N bonds in this complex, which are seemingly slightly more ionic in character.

Conformational Energetics

The ruffled and planar conformers of cationic **1** are not markedly different in energy, as shown by the thermochemical data in Table 3. At 298.15 K, the free energy difference between the conformers is only 2.23 kJ mol^{-1}, with the ruffled conformer being the more stable of the two. Interestingly, the energy order of the conformers is reversed if the *meso*-phenyl groups are replaced with H atoms in the calculations, i.e. *ruf*-[Rh(porphine)($PEtPh_2$)$_2$]$^+$ is *less stable* than *flat*-[Rh(porphine)($PEtPh_2$)$_2$]$^+$ by $\Delta H \approx 0.77$ kJ mol^{-1} at 298.15 K (data not shown). The latter is consistent with an earlier report based on molecular mechanics (MM) calculations that ruffled *metal–porphine conformers* are always more strained than their planar counterparts and that the magnitude of the energy difference increases as a function of the extent of ruffling of the macrocycle.[47] From the data in Table 3, we surmise that nonbonded interactions between the axial phosphane ligands and the *meso*-phenyl groups in the TPP derivative dominate the conformational energetics, at least for the minimum energy conformations shown in Figure 7. A more complete understanding of the potential energy surface (ΔH vs. the two dihedral angles controlling the orientations of the axial phosphane ligands relative to the porphyrin core) could be gained from a surface scan effected by standard dihedral angle driving methods. However, even at the PBE1PBE/3-21G** level of theory, an adequately sampled grid of 37^2 conformers to define the potential energy surface (PES) is computationally highly expensive and well beyond the scope of the present article (though clearly of interest to supercomputer enthusiasts).

Table 3. Thermochemical analysis for the DFT-calculated *ruf* and *flat* conformers of cationic **1** (298.15 K, 1 atm).[a]

	ruf-[Rh(TPP)(L)$_2$]$^+$	*flat*-[Rh(TPP)(L)$_2$]$^+$
E_{elec}	–8323.282868	–8323.281658
ZPE	1.127888	1.127678
Thermal corr. to E_{elec}	1.193132	1.193017
Thermal corr. to H	1.194076	1.193961
Thermal corr. to G	1.024706	1.024346
E_0 (0 K)	–8322.15498	–8322.15398
E (stp)	–8322.089736	–8322.088641
H (stp)	–8322.088792	–8322.087697
G (stp)	–8322.258162	–8322.257312
E_{rel} (0 K)[b]	0	2.626
E_{rel} (stp)[b]	0	2.875
H_{rel} (stp)[b]	0	2.875
G_{rel} (stp)[b]	0	2.232

[a] DFT method = in vacuo PBE1PBE/3-21G**; L = PEtPh$_2$; all energies are in Hartree units unless otherwise noted (1 Hartree = 2625.50 kJ mol^{-1}). The energy parameters E_{elec}, H, G, and ZPE are the electronic energy, enthalpy, Gibbs free energy and zero-point energy, respectively. $E_0 = E_{elec}$ + ZPE; $E = E_0 + E_{vib} + E_{rot} + E_{transl}$, $H = E + RT$; $G = H - TS$; stp = standard temperature (298.15 K) and pressure (1 atm). [b] Relative energy, enthalpy or Gibbs free energy in kJ mol^{-1}.

What we can articulate from the data in Table 3 is that at 298 K, both the ruffled and planar conformers of cationic **1** should have almost equal populations. Our variable-temperature NMR-spectroscopic studies in fact confirm this (a single pyrrole ^{1}H resonance is observed from 253 to 323 K) and indicate a fairly low energy barrier connecting the two stable conformers on the PES. Conformational surfaces of the type discussed above have been computed previously at the MM level of theory with appropriately derived force fields for iron(III)–[48] and cobalt(III)–porphyrin[31] complexes. In these studies, with both sterically compact and bulky porphyrin ligands, in-vacuo potential-energy barriers delineating the pathways that connect ruffled and planar conformers tend to be < 12 kJ mol^{-1}, thus permitting free rotation of the axial ligands at ambient temperature.

Shielding Tensor Determinations

The isotropic shielding tensor (δ_{iso}) for the ^{103}Rh nucleus of **1** was adequately calculated at the PBE1PBE/3-21G** level of theory (Table 4). The shielding tensor determination employing the larger basis set (DGDZVP) afforded a surprisingly poor prediction of δ_{Rh}. This result is somewhat unexpected given the generally good performance of the DGDZVP basis set for geometry optimisations and frequency calculations for most complexes of transition metal ions.[49] Furthermore, the ^{31}P shielding for **1** was considerably more accurately determined relative to that calculated with the 3-21G** basis set. Such a problem can only result from an inherent deficiency in the core electron parameterisation for *heavier nuclei* such as Rh because geometry optimisations and frequency calculations, which are primarily dependent on the accuracy of interactions involving the valence electrons, are not in any way problematic for this basis set.

Table 4. In-vacuo DFT-calculated (PBE1PBE-GIAO method) shielding tensors, diagonal matrix elements and anisotropy parameters (all in ppm) for key conformations of [Rh(TPP)(PEtPh$_2$)$_2$]$^+$.[a]

Atom	δ_{iso}	δ_{xx}	δ_{yy}	δ_{zz}	$\delta_{anisot.}$	Δ_{iso}[d]	Δ'_{iso}[d]
Ruffled (C_1 symmetry)							
Rh[b]	2683	2655	2659	2734	89.9	398	125
Rh[c]	1272	1140	1193	1484	422	–1013	–1286
P[b]	30.49	–42.1	–10.5	144	32.0	20.1	19.7
P[c]	17.6	–4.25	–47.4	104	93.0	7.16	6.77
Planar (C_2 symmetry)							
Rh[b]	2605	2679	2517	2618	119	320	47
P[b]	26.2	–54.4	–33.8	167	22.4	15.8	15.4

[a] NMR reference compounds: ^{103}Rh, [RhCl$_6$]$^{3-}$; ^{31}P, H$_3$PO$_4$. [b] 3-21G** basis set. [c] DGDZVP basis set. [d] Experimental isotropic shielding: $\delta_{Rh} = 2285(5)$ ppm at 0 K ($\delta = 2558$ ppm at 300 K); $\delta_P = 10.40(2)$ ppm at 0 K ($\delta = 10.79$ ppm at 300 K). Δ_{iso} and Δ'_{iso} are the differences between the calculated and experimental isotropic shieldings at 0 and 300 K, respectively.

A noteworthy point concerning the data in Table 4 is that because the DFT simulations were performed in vacuo, the DFT-calculated chemical shifts are compared with the experimental chemical shifts extrapolated to 0 K in the first instance for two reasons. First, the temperature of the system in a vacuum tends towards zero; second, current GIAO-DFT methods on static conformations do not take into account thermal shielding derivatives despite the fact that most nuclei have temperature-dependent isotropic and anisotropic shielding tensors. At 0 K then, the calculated in-vacuo ^{103}Rh chemical shift of *ruf*-[Rh(TPP)(PEtPh$_2$)$_2$]$^+$ is within 20% of the experimental chemical shift for **1** for the calculation with the 3-21G** basis set. At 300 K, the agreement between theory and experiment is even better (5%) but fundamentally unsatisfactory because of the intrinsic temperature difference between the two methods.

Other workers have reported DFT-based GIAO-calculated ^{103}Rh chemical shifts for several Rh^{I} and Rh^{III} coordination compounds that are typically within 300 ppm, or roughly 10–15%, of the experimental chemical shift.[50,51] Our results for **1** are evidently typical for the DFT method employed and show that a relatively small basis set may be used with some measure of confidence for future simulations on this comparatively large-scale problem. Although the GIAO-calculated chemical shifts for ^{103}Rh in **1** were relatively accurate for simulations with the 3-21G** basis set, the ^{31}P chemical shift determinations for the planar and ruffled conformers of the [Rh(TPP)(PEtPh$_2$)$_2$]$^+$ cation were significantly less accurate. As indicated in Table 4, δ_P deviates from the experimental chemical shift by up to 20 ppm. This more than likely highlights shortfalls in the 3-21G** basis set for shielding tensor calculations on light elements, because neither the use of a truncated porphyrin model such as [Rh(porphine)(PEtPh$_2$)^2]$^+$ (Table S3) nor a chloroform solvent model (see below) yielded markedly improved agreement between the calculated and observed chemical shifts. (It is normal to use the much larger 6-311G** basis set for accurate GIAO simulations on H through Kr, computational resources permitting.) Whereas the accuracy of

GIAO calculations with large basis sets tends to be rather good for organic compounds, it is quite clear that in the presence of transition metal ions, δ_P predictions with large basis sets are typically only accurate to within 10–25 ppm of the experimental chemical shift[52–54] and therefore no better than those employing the 3-21G** basis set reported here.

The NMR shielding tensor determinations for the ruffled and planar conformers of **1** were also calculated in a chloroform solvent continuum (PCM method,[55] Table S4) in an effort to gauge the solvent contribution to the chemical shifts. Because the ^{103}Rh and ^{31}P nuclei of **1** are deeply buried within the framework of a large molecule, the presence of the solvent had a negligible effect on the calculated isotropic shielding values for these two nuclei. Thus, δ_{Rh} and δ_P computed in a chloroform polarisation continuum were 1% worse and 1.5% better compared with the experimental chemical shifts of these nuclei, respectively. Interestingly, and as noted earlier, use of a truncated porphyrin model such as [Rh(porphine)(PEtPh$_2$)$_2$]$^+$ (Table S3) had practically no effect on the accuracy of the calculated ^{31}P chemical shifts. The calculated ^{103}Rh chemical shifts were, on the other hand, closer to the experimental values for **1** (this improvement for the truncated structural model is of course counter-intuitive). The *meso*-phenyl groups of the porphyrin ligand are evidently not inconsequential to the electronic structure of the compound, and it is clear that an Rh^{III} complex as large as **1** presents a formidable challenge for current DFT and GIAO theory that we have not yet satisfactorily met with the present PBE1PBE/3-21G** simulations. The problem is that very few all-electron basis sets for heavy nuclei suitable for conducting nuclear shielding calculations have been developed.

Conclusions

We have synthesised and characterised a novel ruffled Rh^{III}–porphyrin bearing moderately bulky axial PEtPh$_2$ ligands as its hexafluoroantimonate(V) salt, [Rh(TPP)(PEtPh$_2$)$_2$]SbF$_6$. Indirect detection of the ^{103}Rh NMR signal by means of polarisation transfer from ^{31}P has enabled us to gauge the nuclear shielding of the rhodium ion as a function of temperature – a first for Rh^{III}–porphyrins. DFT simulations at the PBE1PBE/3-21G** level of theory were surprisingly accurate for the coordination geometry of the metal ion and porphyrin ligand and moderately accurate at prediction of the ^{103}Rh isotropic shielding tensor. We are currently extending this study to include several bis(phosphane)-, bis(phosphinite)- and bis(phosphonite)Rh^{III}–porphyrins in an effort to establish empirical correlations between δ_{Rh}, $J_{(P,Rh)}$ and parameters derived from X-ray crystal structures of these stable, yet conformationally flexible compounds.

Experimental Section

General: All manipulations were carried out under nitrogen by using a double manifold vacuum line, Schlenk and cannula techniques. THF and hexane were distilled from sodium/benzophenone. Dichloromethane and pyrrole (Aldrich) were distilled from CaH_2. Benzaldehyde, silver hexafluoroantimonate(V) and ethyldiphenylphosphane (PEtPh$_2$) were used as received (Aldrich). H_2TPP was synthesised according to published procedures.[56] [Rh(TPP)Cl] was prepared by metallation of H_2TPP with rhodium(III) chloride in DMF heated to reflux.[57]

Instrumental Methods: Electronic spectra were recorded with a Shimadzu UV-1800 double-beam scanning spectrophotometer by using dry dichloromethane solutions prepared from single crystals of **1** without excess phosphane in a 1.0 cm path-length quartz cuvette. FTIR spectra of one or more single crystals of **1** were recorded with a Bruker Alpha diamond ATR spectrometer (48 scans, spectroscopic resolution = 1.0 cm^{-1}). C, H and N elemental analysis (combustion) data were obtained from Galbraith Laboratories (USA) on a polycrystalline sample of **1**.

Synthesis of 1: To [Rh(TPP)Cl] (150 mg, 0.20 mmol) and $AgSbF_6$ (82 mg, 0.24 mmol) in a 250 mL Schlenk tube under nitrogen was added freshly distilled THF (50 mL). The solution was stirred at room temperature for ca. 12 h. The THF was then removed in vacuo and the green-brown solid redissolved in dichloromethane (50 mL). The solution was then filtered, to remove precipitated silver chloride, into a 250 mL Schlenk tube into which PEtPh$_2$ (0.82 mL, 4.0 mmol) had been added. The solution was stirred at room temperature for ca. 10 min. The purple-red solution was then transferred into 12 Schlenk tubes in ca. 4 mL aliquots and layered with hexane. X-ray-quality crystals were observed after 4 d. Isolated yield: 0.2532 g (92%). $C_{74}H_{62}Cl_4F_6N_4P_2RhSb$ (1549.76): calcd. C 57.35, H 4.03, N 3.62; found C 56.80, H 4.48, N 4.19. ^{1}H NMR (500 MHz, $CDCl_3$, 298 K): δ = 8.78 (s, 8 H, pyrrole β-H), 7.76 (m, 20 H, TPP *o*-, *m*-, *p*-H), 7.01 (t, ^3J = 7.3 Hz, 4 H, L *p*-H), 6.57 (t, ^3J = 7.5 Hz, 8 H, L *m*-H), 3.73 (p, ^3J = 3.8 Hz, 8 H, L *o*-H), –1.40 (p, ^3J = 7.7 Hz, 6 H, CH_3), –2.84 (q, ^3J = 7.7 Hz, 4 H, CH_2) ppm. ^{13}C{^{1}H} NMR (125 MHz, $CDCl_3$, 298 K): δ = 142.494 (TPP C_a), 142.074 (TPP C_a), 140.913 (TPP C_a), 140.842 (TPP C_a), 140.691 (C_m-C_{phenyl}), 137.913 (TPP C_b), 137.844 (TPP C_b), 134.360, 134.238, 134.112, 133.253, 133.092, 132.831, 132.639, 132.499, 132.257, 131.589, 131.570, 130.763, 130.690, 128.567, 128.353, 128.300, 127.048 (P-C_{phenyl}), 126.943, 126.742 (P-C_{phenyl}), 122.26 (TPP C_m), 121.994 (TPP C_m), 20.543 (CH_2), 20.483 (CH_2), 9.933 (CH_3) ppm. IR (crystalline solid): $\tilde{\nu}$ = 518, [m, ν(Rh–P)], 652 [s, ν(P–Et)], 1012 [s, ν(C=C) porphyrin], 1439 [w, ν(P–Ph)] cm^{-1} (s, m, w = strong, medium, weak). UV/Vis CH_2Cl_2 at 298 K (ε): λ = 597 [2.78(7) × 10^4], 557 [2.45(4) × 10^4], 515 [1.16(9) × 10^4], 448 [3.35(14) × 10^5], 367 [8.40(24) × 10^4], 308 [7.47(20) × 10^4 M^{-1} cm^{-1}] nm.

Crystallography: X-ray data were collected on a red crystal of the compound with dimensions 0.38 × 0.40 × 0.50 mm by using an Enraf–Nonius CAD4 diffractometer operating at 1.65 kW X-ray power (Mo-K_α radiation, λ = 0.71073 Å) with a Bruker LT3 low-temperature attachment. The data were reduced by using XCAD4[58] and the structure solved with SHELXS-97[59] (running under WinGX[60]) by using direct methods. The structure was refined with SHELXL-97.[61] All non-hydrogen atoms were refined anisotropically, and H atom coordinates were calculated by using the standard riding model of SHELXL. Towards the end of the structure refinement for **1**, it became clear that the phenyl group appended to *meso*-C4 (C4m) was disordered about two orientations. A model, in which two orientations for this phenyl group were present, gave a satisfactory and stable refinement upon fixing the geometry of each component ring to a regular hexagon (AFIX 66 command in SHELXL). Crystallographic data for **1**·2CH_2Cl_2:

$C_{74}H_{62}Cl_4F_6N_4P_2RhSb$ (1549.68 g mol^{-1}), monoclinic, space group $P2_1/n$, a = 17.678(5), b = 17.747(7), c = 22.173(6) Å, β = 106.52(2)°, V = 6669(4) Å^3, Z = 4, D_c = 1.543 g mL^{-1}, μ = 0.925 mm^{-1}, T = 259(2) K, 14060 total reflections, 11689 independent reflections (R_{int} = 0.0168), 9815 reflections with $I > 2\sigma(I)$, R_1 = 0.0535, wR_2 = 0.1476 [for $I > 2\sigma(I)$]. CCDC-223496 contains the supplementary crystallographic details for **1** in CIF format. These data can be obtained free of charge from The Cambridge Crystallographic Data Centre via www.ccdc.cam.ac.uk/data_request/cif.

NMR Spectroscopy: ^{1}H, ^{13}C and ^{31}P NMR spectra of **1** were recorded by using ca. 6–10 mg of polycrystalline material dissolved in 0.60 mL of dry $CDCl_3$ under nitrogen. Data were acquired with a 500 MHz Varian Unity Inova spectrometer equipped with an Oxford magnet (11.744 T) at 298 K. Standard ^{1}H, ^{13}C and ^{31}P pulse sequences were used for 1D and 2D spectra. ^{103}Rh NMR spectra were recorded at 213, 300 and 333 K with a Bruker DRX 400 spectrometer equipped with a 5 mm triple-resonance inverse probe with a dedicated ^{31}P channel and extended decoupler range, operating at 161.98 MHz (^{31}P) and 12.65 MHz (^{103}Rh). Samples were prepared by dissolving 6 mg of polycrystalline material in 0.55 mL of $CDCl_3$ under nitrogen. 2D ^{103}Rh-^{31}P spectra were obtained by using the pulse sequence[61] $\pi/2(^{31}P)$–$1/[2J(^{103}Rh\text{-}^{31}P)]$–$\pi/2(^{103}Rh)$–$\tau$–$\pi(^{31}P)$–$\tau$–$\pi/2(^{103}Rh)$–Acq(^{31}P). A spectroscopic width in $f2$ (^{31}P) of 8 ppm and an acquisition time of 0.396 s gave a digital resolution of 1.26 Hz per point; in $f1$ (^{103}Rh), a spectroscopic width of 40 ppm and a time domain of 256 (reduced, for spectra of the minor component to 60) gave, after zero filling, a digital resolution of 0.49 Hz per point. With a relaxation delay of 2 s and 4 scans per increment, the data collection required 27 min. To eliminate the possibility of a folded signal in $f1$, the spectra were first recorded with a spectroscopic width of 2000 ppm. Chemical shifts were referenced to the generally accepted standards of H_3PO_4 and $\Xi(^{103}Rh)$ = 3.16 MHz[19] with positive values indicating deshielding. The chemical shift of H_3PO_4 (85%, 300 K) with a $CDCl_3$ external lock corresponds to a frequency of 161.975491 MHz in a field (4.395 T) in which the protons of TMS (in CD_2Cl_2 at 300 K) resonate at 400.130020 MHz.

DFT Simulations: All calculations were performed with Gaussian 03W.[62] Input atomic coordinates were either Cartesian coordinates derived from the fractional atomic coordinates of the X-ray structure of **1** or structures prepared with GausView 3.09.[63] The DFT method employed (PBE1PBE) was the gradient-corrected hybrid method of Perdew et al.[42] with either the DGDZVP[44] or 3-21G**[43] basis sets. Frequency calculations were performed on geometry-optimised structures to establish the nature of the stationary points located on the potential energy surface for each structure/conformer. All structures reported in this paper were stable minima (no frequency eigenvalues < 0). Shielding tensors were determined by the GIAO method[45] on the optimised 3-21G** geometries. Chemical shifts were determined by using calculated shielding tensors for H_3PO_4 and $[RhCl_6]^{3-}$ as the ^{31}P and ^{103}Rh reference compounds, respectively. In order to compare our experimental ^{103}Rh chemical shifts (which are referenced to metallic rhodium) with those obtained by the GIAO theory, a correction factor of –4819.1 ppm was used. This factor corresponds to the difference between δ_{Rh} calculated for $[RhCl_6]^{3-}$ at the PBE1PBE/3-21G** level of theory (–12819.1 ppm) and the chemical shift value (–8000 ppm) needed to zero the experimental chemical shift of $[RhCl_6]^{3-}$ (+8000 ppm relative to metallic rhodium).

Supporting Information (see footnote on the first page of this article): Figures S1 and S2, additional electronic spectra; Figures S3a and 3b, ^{1}H NMR spectra for the water protons of $[Rh(TPP)(OH_2)(PEtPh_2)]SbF_6$ and **1** as a function of temperature, respectively; Figures S4–S6, additional X-ray structure diagrams; Figure S7, frontier MOs for cationic **1**; Figure S8, Cartesian axes for conformers of cationic **1**; Figure S9, calculated geometry of $[Rh(TPP)(OH_2)(PEtPh_2)]^+$; Figure S10, ^{1}H NMR spectroscopic data for of $[Rh(TPP)(PHEtPh)(PEtPh_2)]^+$; Tables S1–S6, additional experimental and theoretical numerical data.

Acknowledgments

The authors thank the National Research Foundation of South Africa (NRF, Pretoria), the University of the Witwatersrand and the University of KwaZulu-Natal for financial support. We are also especially indebted to Mr. Craig Grimmer for recording some of the variable-temperature ^{1}H and ^{31}P NMR spectroscopic data in this work and Wen Wen Suo for her contribution to sample preparations.

[1] Abbreviations: DFT = density functional theory, esd = estimated standard deviation, GIAO = gauge-independent atomic orbitals; TF5PP = dianion of 5,10,15,20-tetrakis(pentafluorophenyl)porphyrin, TPP = dianion of 5,10,15,20-tetraphenylporphyrin, OEP = 2,3,7,8,12,13,17,18-octaethylporphyrin dianion, 1-MepipZ = 1-methylpiperazine, THF = tetrahydrofuran; nd = not determined.

[2] S. Ariel, D. Dolphin, G. Domazetis, B. R. James, T. W. Leung, S. J. Rettig, J. Trotter, G. M. Williams, *Can. J. Chem.* **1984**, *62*, 755–762.

[3] B. R. James, D. Dolphin, T. W. Leung, F. W. B. Einstein, A. C. Willis, *Can. J. Chem.* **1984**, *62*, 1238–1245.

[4] C.-M. Che, J.-L. Zhang, R. Zhang, J.-S. Huang, T.-S. Lai, W.-M. Tsui, X.-G. Zhou, Z.-Y. Zhou, N. Zhu, C. K. Chang, *Chem. Eur. J.* **2005**, *11*, 7040–7053.

[5] E. Stulz, M. Maue, N. Feeder, S. J. Teat, Y.-F. Ng, A. D. Bond, S. L. Darling, J. K. M. Sanders, *Inorg. Chem.* **2002**, *41*, 5255–5268.

[6] R. M. Belani, B. R. James, D. Dolphin, S. J. Rettig, *Can. J. Chem.* **1988**, *66*, 2072–2078.

[7] L. Toupet, N. Legrand, A. Bondon, G. Simonneaux, *Acta Crystallogr., Sect. C* **1994**, *50*, 1014–1016.

[8] M.-A. Pilard, M. Guillemot, L. Toupet, J. Jordanov, G. Simonneaux, *Inorg. Chem.* **1997**, *36*, 6307–6314.

[9] L. Toupet, P. Sodano, G. Simonneaux, *Acta Crystallogr., Sect. C* **1990**, *46*, 1631–1633.

[10] a) C.-M. Che, T.-F. Lai, W.-C. Chung, W. P. Schaefer, H. B. Gray, *Inorg. Chem.* **1987**, *26*, 3907–3911; b) J. Xie, J.-S. Huang, N. Zhu, Z.-Y. Zhou, C.-M. Che, *Chem. Eur. J.* **2005**, *11*, 2405–2416.

[11] a) K. M. Kadish, J.-L. Cornillon, P. Mitaine, Y. J. Deng, J. D. Korp, *Inorg. Chem.* **1989**, *28*, 2534–2542; b) K. M. Kadish, Y. J. Deng, J. D. Korp, *Inorg. Chem.* **1990**, *29*, 1036–1042.

[12] Cambridge Structural Database (CSD), version 5.29 (July 2008); F. H. Allen, *Acta Crystallogr., Sect. B* **2002**, *58*, 380–388.

[13] a) E. Stulz, S. M. Scott, Y.-F. Ng, A. D. Bond, S. J. Teat, S. L. Darling, N. Feeder, J. K. M. Sanders, *Inorg. Chem.* **2003**, *42*, 6564–6574; b) K. Fukushima, K. Funatsu, A. Ichimura, Y. Sasaki, M. Suzuki, T. Fujihara, K. Tsuge, T. Imamura, *Inorg. Chem.* **2003**, *42*, 3187–3193; c) E. Stulz, S. M. Scott, A. D. Bond, S. J. Teat, J. K. M. Sanders, *Chem. Eur. J.* **2003**, *9*, 6039–6048.

[14] B. B. Wayland, B. A. Woods, V. M. Minda, *J. Chem. Soc., Chem. Commun.* **1982**, 634–635.

[15] X. Li, R. Irie, S. Shinoda, Y. Saito, *Nippon Kagaku Kaishi* **1984**, 271–276.

[16] a) H. J. Callot, C. Piechocki, *Tetrahedron Lett.* **1980**, *21*, 3489–3492; b) H. J. Callot, F. Metz, C. Piechocki, *Tetrahedron* **1982**,

38, 2365–2369; c) H. J. Callot, F. Metz, *Nouv. J. Chim.* **1985**, *9*, 167–171.
[17] a) K. M. Kadish, Y. Hu, T. Boschi, P. Tagliatesta, *Inorg. Chem.* **1993**, *32*, 2996–3002; b) R. Guilard, K. M. Kadish, *Chem. Rev.* **1988**, *88*, 1121–1146.
[18] ^{103}Rh NMR studies of Rh^{I} and Rh^{III} complexes in general include the following works: a) M. Soleilhavoup, L. Viau, G. Commenges, C. Lepetit, R. Chauvin, *Eur. J. Inorg. Chem.* **2003**, *2*, 207–212; b) M. Herberhold, H. Yan, W. Milius, B. Wrackmeyer, *Chem. Eur. J.* **2002**, *8*, 388–395; c) S. Haep, M. Nieger, D. Gudat, M. Betke-Hornfeck, D. Schramm, *Organometallics* **2001**, *20*, 2679–2685.
[19] R. G. Kidd, R. J. Goodfellow, in *NMR and the Periodic Table* (Eds.: R. K. Harris, B. E. Mann), Academic Press, New York, **1978**, pp. 195–278.
[20] J. R. Houston, M. M. Olmstead, W. H. Casey, *Inorg. Chem.* **2006**, *45*, 7799–7805.
[21] D. J. Law, G. Bigam, R. G. Cavell, *Can. J. Chem.* **1995**, *73*, 635–642.
[22] a) B. R. Bender, M. Koller, D. Nanz, W. von Philipsborn, *J. Am. Chem. Soc.* **1993**, *115*, 5889–5890; b) L. Carlton, *Magn. Reson. Chem.* **1997**, 35,153–158; c) W. von Philipsborn, *Chem. Soc. Rev.* **1999**, *28*, 95–105; d) M. Herberhold, H. Yan, W. Milius, B. Wrackmeyer, *Chem. Eur. J.* **2002**, *8*, 388–395.
[23] T. Boschi, S. Licoccia, P. Tagliatesta, *Inorg. Chim. Acta* **1987**, *126*, 157–160.
[24] W. R. Scheidt, Y. J. Lee, *Struct. Bonding (Berlin)* **1987**, *64*, 1–70.
[25] B. A. Kelly, A. J. Welch, P. Woodward, *J. Chem. Soc., Dalton Trans.* **1977**, 2237–2242.
[26] E. Stulz, S. M. Scott, A. D. Bond, S. Otto, J. K. M. Sanders, *Inorg. Chem.* **2003**, *42*, 3086–3096.
[27] D. C. Thackray, S. Ariel, T. W. Leung, K. Menon, B. R. James, J. Trotter, *Can. J. Chem.* **1986**, *64*, 2440–2446.
[28] C. A. Tolman, *Chem. Rev.* **1977**, *77*, 313–348.
[29] The relevant nonbonded contacts include C4a···C52 (3.197 Å), N2···C52 (3.275 Å), C1a···C66 (3.334 Å), and N1···C61 (3.298 Å) for the uppermost axial ligand in Figure 1.
[30] O. Q. Munro, S. C. Shabalala, N. J. Brown, *Inorg. Chem.* **2001**, *40*, 3303–3317.
[31] A. J. Parusel, S. Grimme, *J. Porphyrins Phthalocyanines* **2001**, *5*, 1–8.
[32] I.-K. Choi, Y. Liu, Z. Wei, M. D. Ryan, *Inorg. Chem.* **1997**, *36*, 3113–3118.
[33] A. Bax, R. H. Griffey, B. L. Hawkins, *J. Am. Chem. Soc.* **1983**, *105*, 7188–7190.
[34] W. von Philipsborn, *Chem. Soc. Rev.* **1999**, *28*, 95–105.
[35] H. C. E. McFarlane, W. McFarlane, R. J. Wood, *Bull. Soc. Chim. Belg.* **1976**, *85*, 864–871.
[36] L. Öhrström, *Comments Inorg. Chem.* **1996**, *18*, 305–323.
[37] T. H. Brown, P. J. Green, *J. Am. Chem. Soc.* **1970**, *92*, 2359–2362.
[38] P. S. Pregosin, R. W. Kunz, "^{31}P and ^{13}C NMR of Transition Metal Phosphine Complexes" in *NMR 16*, *Basic Principles and Progress* (Eds.: P. Diehl, E. Fluck, R. Kosfeld), Springer-Verlag, Berlin, **1979**, pp. 47–49.
[39] C. J. Jameson, D. Rehder, M. Hoch, *J. Am. Chem. Soc.* **1987**, *109*, 2589–2594.
[40] J. P. Perdew, K. Burke, M. Ernzerhof, *Phys. Rev. Lett.* **1996**, *77*, 3865–3868.
[41] R. Ditchfield, W. J. Hehre, J. A. Pople, *J. Chem. Phys.* **1971**, *54*, 724–728.
[42] N. Godbout, D. R. Salahub, J. Andzelm, E. Wimmer, *Can. J. Chem.* **1992**, *70*, 560–571.
[43] K. Ruud, T. Helgaker, K. L. Bak, P. Jørgensen, H. J. A. Jensen, *J. Chem. Phys.* **1993**, *99*, 3847–3859.
[44] a) O. Q. Munro, H. M. Marques, P. G. Debrunner, K. Mohanrao, W. R. Scheidt, *J. Am. Chem. Soc.* **1995**, *117*, 935–954; b) O. Q. Munro, P. S. Madlala, R. A. F. Warby, T. S. Seda, G. Hearne, *Inorg. Chem.* **1999**, *38*, 4724–4736.
[45] J. E. Carpenter, F. Weinhold, *THEOCHEM* **1988**, *169*, 41–62.
[46] F. A. Walker, in *The Porphyrin Handbook* (Eds.: K. M. Kadish, K. M. Smith, R. Guilard), Academic Press, San Diego, **2000**, vol. 5, pp. 81–183.
[47] O. Q. Munro, J. C. Bradley, R. D. Hancock, H. M. Marques, F. Marsicano, P. W. Wade, *J. Am. Chem. Soc.* **1992**, *114*, 7218–7230.
[48] O. Q. Munro, J. A. Serth-Guzzo, I. Turowska-Tyrk, K. Mohanrao, T. K. Shokhireva, F. A. Walker, P. G. Debrunner, W. R. Scheidt, *J. Am. Chem. Soc.* **1999**, *121*, 11144–11155.
[49] C. Sosa, J. Andzelm, B. C. Elkin, E. Wimmer, K. D. Dobbs, D. A. Dixon, *J. Phys. Chem.* **1992**, *96*, 6630–6636.
[50] M. Bühl, M. Håkansson, A. H. Mahmoudkhani, L. Öhrstrom, *Organometallics* **2000**, *19*, 5589–5596.
[51] M. Bühl, *Chem. Phys. Lett.* **1997**, *267*, 251–257.
[52] X. Xu, L. Fang, Z.-X. Chen, G.-C. Yang, S.-L. Sun, Z.-M. Su, *J. Organomet. Chem.* **2006**, *691*, 1927–1933.
[53] Y. Ruiz-Morales, T. Ziegler, *J. Phys. Chem. A* **1998**, *102*, 3970–3976.
[54] K. Eichele, R. E. Wasylishen, J. F. Corrigan, N. J. Taylor, A. J. Carty, K. W. Feindel, G. M. Bernard, *J. Am. Chem. Soc.* **2002**, *124*, 1541–1552.
[55] M. Cossi, G. Scalmani, N. Rega, V. Barone, *J. Chem. Phys.* **2002**, *117*, 43–54.
[56] G. H. Barnett, M. F. Hudson, K. M. Smith, *J. Chem. Soc. Perkin Trans. 1* **1975**, 1401–1403.
[57] A. D. Adler, F. R. Longo, F. Kampas, J. Kim, *J. Inorg. Nucl. Chem.* **1970**, *32*, 2443–2445.
[58] K. Harms, S. Wocadlo, *XCAD4 – Program for Processing CAD4 Diffractometer Data*, University of Marburg, Germany, **1995**.
[59] G. M. Sheldrick, *SHELXS-97 and SHELXL-97 – Programs for Crystal Structure Solution and Refinement*, release 97-2, University of Göttingen, Germany, **1997**.
[60] L. J. Farrugia, *J. Appl. Crystallogr.* **1999**, *32*, 837–838.
[61] A. Bax, R. H. Griffey, B. L. Hawkins, *J. Magn. Reson.* **1983**, *55*, 301–315.
[62] M. J. Frisch, G. W. Trucks, H. B. Schlegel, G. E. Scuseria, M. A. Robb, J. R. Cheeseman, V. G. Zakrzewski, J. A. Montgomery, R. E. Stratmann, J. C. Burant, S. Dapprich, J. M. Millam, A. D. Daniels, K. N. Kudin, M. C. Strain, O. Farkas, J. Tomasi, V. Barone, M. Cossi, R. Cammi, B. Mennucci, C. Pomelli, C. Adamo, S. Clifford, J. Ochterski, G. A. Petersson, P. Y. Ayala, Q. Cui, K. Morokuma, D. K. Malick, A. D. Rabuck, K. Raghavachari, J. B. Foresman, J. Cioslowski, J. V. Ortiz, B. B. Stefanov, G. Liu, A. Liashenko, P. Piskorz, I. Komaromi, R. Gomperts, R. L. Martin, D. J. Fox, T. Keith, M. A. Al-Laham, C. Y. Peng, A. Nanayakkara, C. Gonzalez, M. Challacombe, P. M. W. Gill, B. G. Johnson, W. Chen, M. W. Wong, J. L. Andres, M. Head-Gordon, E. S. Replogle, J. A. Pople, *Gaussian 03*, revision D.01, Gaussian, Inc., Pittsburgh PA, **2004**.
[63] *GausView 3.09, Graphical Interface to Gaussian 03*, Gaussian Inc., Carnegie Office Park, Building 6, Pittsburgh PA 15106, USA, http://www.gaussian.com.
[64] L. J. Farrugia, *J. Appl. Crystallogr.* **1997**, *30*, 565–565.
[65] The root mean square fit employed the Rh atom, axial P atoms and 24 porphyrin core atoms from each structure.

Received: August 21, 2008
Published Online: Aoril 29, 2009

